ST-ECF Instrument Science Report ACS-2006-02

Wavelength and Flux calibration of the ACS/SBC PR110L and PR130L prisms

S. S. Larsen, February 2006

ABSTRACT

Wavelength- and flux calibrations are presented for the ACS/SBC PR110L and PR130L slitless spectroscopy modes. The calibrations were derived from Cycle 13 observations of two QSOs at redshift z=0.098 and z=0.168 (for the wavelength calibration) and two white dwarf standards (for the flux calibration), and are made available to users as configuration files for the aXe software package. Both the trace- and wavelength solutions include spatial variations across the SBC detector, and flat-fields (compatible with the aXe flat-field cube format) are provided to correct for the detected large-scale sensitivity variations. Shifts between direct images obtained in different passbands are also quantified, and corrections relative to the reference (F165LP) passband are given.

Introduction

The ACS has three prisms: two in the Solar Blind Channel (PR110L and PR130L), and one in the High Resolution Channel (PR200L). The initial ground calibrations of the ACS prisms (and grism) are described in Bohlin et al. (2000). Due to the recent increase in the interest in the slitless prism spectroscopy modes on the Advanced Camera for Surveys (largely because of STIS being unavailable), an extensive effort was made in Cycle 13 to provide improved, up-to-date calibration products. This ISR describes the in-orbit wavelength- and flux calibration of the SBC prisms, while the calibration of the PR200L is discussed separately (Larsen et al. 2006). The calibration products described here are tailored for use with the aXe spectral extraction package (Kümmel et al. 2005) and are available to users via the aXe web page (http://www.stecf.org/software/aXe).

The two prisms in the SBC cover roughly the same region of the spectrum, from ~1200 Å to ~2000Å, at similar spectral resolution and sensitivity, the main difference between them being that the coverage of the PR110L extends below 1216Å. Extending the sensitivity to shorter wavelengths comes at the cost of higher sky background, due to the geocoronal Ly α emission. Thus, unless coverage below ~1250 Å is important for the science goals, most users will probably prefer the PR130L. This is especially true since

photon noise is always the dominant noise source for prism spectroscopy with the SBC MAMA, which has no read noise.

Data

As for the other slitless spectroscopy modes on ACS, observations with the SBC prisms generally consist of a direct image which is used to establish the zero-point of the wavelength scale, followed by one or more exposures through the dispersing element (prism). From the observers perspective, the main difference between the SBC and other modes is the bright object protection (BOP) limit which must be satisfied in *both* the prism and direct images in order to avoid damaging the MAMA detector. Thus, targets for which the count rate remains below the BOP limit in the prism exposures may still be too bright in the direct image for certain filter choices.

Various types of objects have been considered for in-orbit wavelength calibration of HST slitless spectroscopy modes, including planetary nebulae, Wolf-Rayet stars and quasars (see Pasquali et al. 2006 for a detailed discussion). Due to the low dispersion of the prisms and the high spatial resolution of the SBC, the calibrator targets must exhibit strong emission lines with large equivalent widths in the wavelength range of interest, and at the same time be compact (preferably with angular diameter < 1 pixel, or 0.03”). Observations of a planetary nebula in the LMC (LMC-SMP-81) were carried out as part of the INTERIM calibration program (Cycle 11, Progr. 9672, P.I. Pasquali), but these spectra turned out to be dominated by the continuum with hardly any identifiable lines. In addition, most PNe in the LMC have larger diameters than desirable, typically several tenths of an arcsec. Thus, for the Cycle 13 observations we decided to rely solely on QSOs for the SBC wavelength calibrations.

The QSOs were selected from the catalog of Veron-Cetty & Veron (2003), which lists nearly 50000 QSOs with redshifts up to 6.4 and makes it possible to select QSOs with emission features at essentially any desired wavelength. We selected the two QSOs PG1322+659 (z=0.168) and PG1404+226 (z=0.098). At these redshifts, Ly α appears at 1420Å and 1335Å, and C IV is at 1806Å and 1701Å in the two QSOs, respectively. Both targets are located in regions of low foreground extinction with A_B = 0.081 mag for PG1322+659 and A_B=0.096 for PG1404+226, according to the extinction maps of Schlegel et al. (1998). An additional selection criterion was that the QSOs had to be fainter than V=15 mag in order to satisfy the BOP limit. For the flux calibration we used the two white dwarf standards WD1657+343 and LDS749B, for which STIS spectra were kindly provided by R. Bohlin.

The observations were carried out under program 10391 (P.I. Larsen) between the dates of 2005-04-18 and 2005-08-08. Each target was observed at a minimum of 5 positions across the SBC detector in order to map spatial variations in the traces, wavelength solutions and sensitivity. As illustrated in Figure 1, one of the QSOs (PG1322+659) was

observed at 10 positions across the detector. The summed PR110L and PR130L exposures are shown at the same contrast setting in the two panels, and the much higher sky background in PR110L (by about a factor of 10) is easily appreciated. Also note that about 200 columns of the MAMA detector (to the right) are vignetted. This vignetting is taken into account in the definition of the default prism apertures, which are centered on the unvignetted part of the detector. Note that the "center" of the SBC MAMA is formally defined to be at (x,y) = (512, 400), in order to avoid a few defect rows near y=600.

A log of the observations is given in Table 1 which lists the POS-TARG offsets with respect to the default aperture center for each observation, together with the filter used for the direct image and the exposure times of the direct imaging and prism exposures. Direct images were typically taken in the F165LP filter, since this filter resulted in the lowest count rates for the QSO targets which were otherwise uncomfortably close to the BOP limit. One target, LDS749B was observed in both F165LP and F122M in order to test whether any spatial offsets were present between images taken in different bands. As discussed further below, such offsets were indeed found. Some objects were observed at two positions near the center of the field, separated by a small (0.015 arcsec) dither. This allowed a check of how sub-pixel shifts might affect the flux- and wavelength calibrations.

Exposure times were between 15 s and 30 s for the direct images, and 35 s - 120 s for the prism exposures (see Table 1 for details). Contrary to the standard procedure for the CCD detectors in ACS, the SBC exposures were not split into multiple exposures since the SBC MAMA is not affected by cosmic-ray hits.

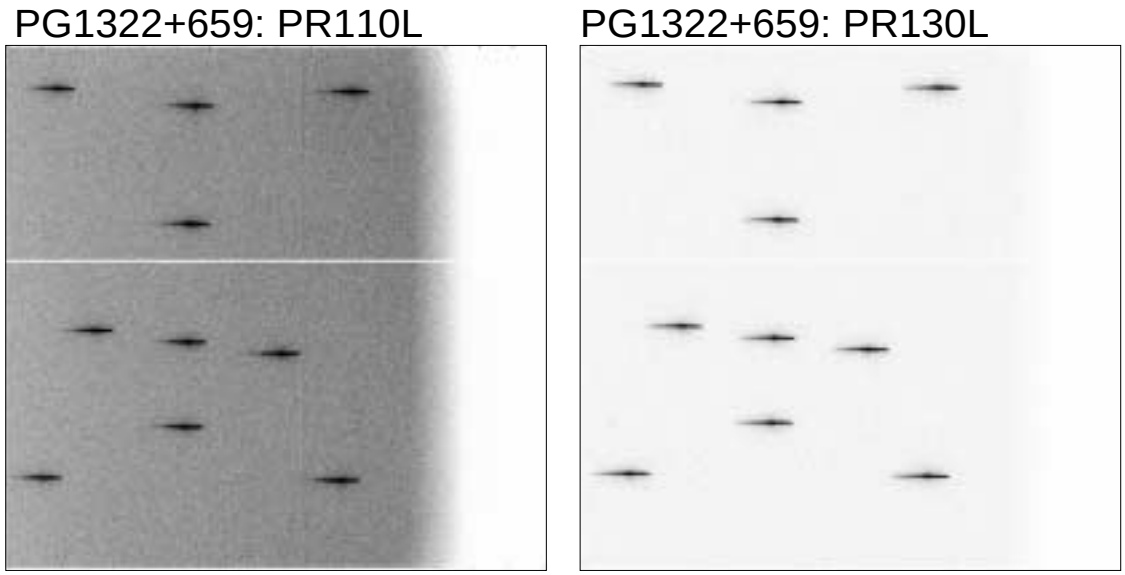

Figure 1: Sum of the 10 exposures in PR110L (left) and PR130L (right) of PG1322+659. The two images are shown at the same contrast settings. Note the much higher sky background in PR110L, due to the sensitivity shortwards of 1250 Å.

Table 1. Log of observations.

Target	POS-TARG x (arcsec)	POS-TARG y (arcsec)	Filter (Direct)	T_{exp} (Dir.) (s)	T_{exp} (PR110L) (s)	T_{exp} (PR130L) (s)
PG1322+659	10	-7	F165LP	30	120	120
PG1322+659	6	0	F165LP	30	120	120
PG1322+659	0	-5	F165LP	30	120	120
PG1322+659	0	0	F165LP	30	120	120
PG1322+659	-6	0	F165LP	30	120	120
PG1322+659	-9	-9	F165LP	30	120	120
PG1322+659	10	16	F165LP	30	120	120
PG1322+659	0	7	F165LP	30	120	120
PG1322+659	-9	14	F165LP	30	120	120
PG1322+659	0	0	F165LP	30	120	120
PG1322+659	0.015	0	F165LP	30	120	120
PG1322+659	0	14	F165LP	30	120	120
PG1404+226	0	0	F165LP	30	90	90
PG1404+226	10	-7	F165LP	30	90	90
PG1404+226	-9	-9	F165LP	30	90	90
PG1404+226	10	16	F165LP	30	90	90
PG1404+226	-9	14	F165LP	30	90	90
PG1404+226	0	0	F165LP	30	90	90
WD1657+343	0	0	F122M	15	45	45
WD1657+343	10	-7	F122M	15	45	45
WD1657+343	-9	-9	F122M	15	45	45
WD1657+343	10	16	F122M	15	45	45
WD1657+343	-9	14	F122M	15	45	45
WD1657+343	0.015	0	F122M	15	45	45
WD1657+343	0.0	7	F122M	15	45	45
LDS749B	0	0	F165LP,F122M	15,15	35	35
LDS749B	10	-7	F165LP,F122M	15,15	35	35
LDS749B	-9	-9	F165LP,F122M	15,15	35	35
LDS749B	10	16	F165LP,F122M	15,15	35	35
LDS749B	-9	14	F165LP,F122M	15,15	35	35
LDS749B	0.015	0.0	F165LP,F122M	15,15	35	35

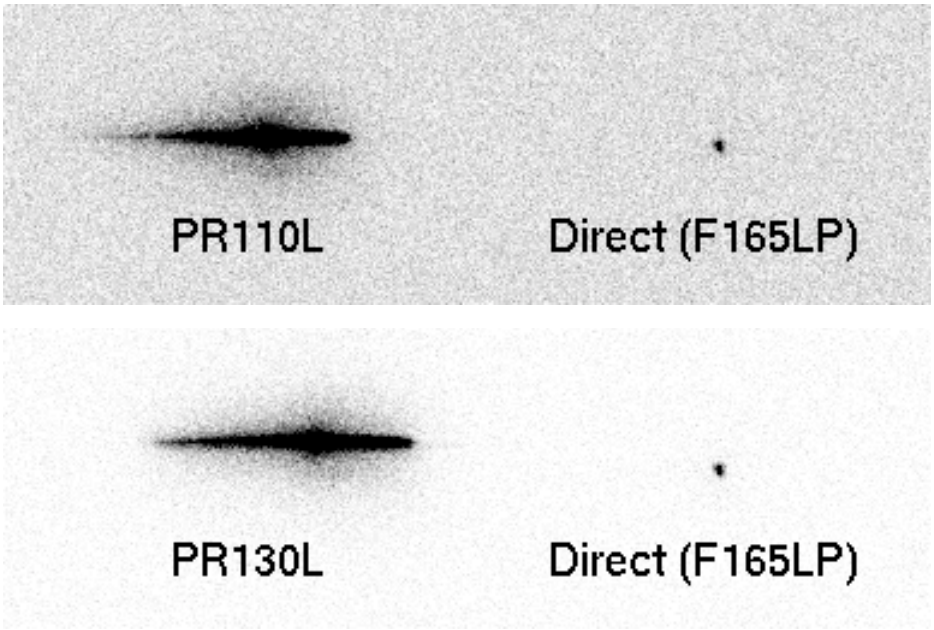

Figure 2: Sum of direct (F165LP) and prism exposures. The top and bottom panels illustrate the location of the PR110L and PR130L prism spectra with respect to the direct image. A slight curvature is present in the PR130L spectra.

Initial data processing and extraction of spectra

Following standard on-the-fly pipeline processing, the first step was to define a configuration file for aXe to allow extraction of the spectra. The location of the spectral trace is defined relative to the position of the object in the direct (F165LP) image, and is of the form $(Y-Y_{ref})$= DYDX_A_0 + DYDX_A_1 * $(X-X_{ref})$ + DYDX_A_2 * $(X-X_{ref})^2$ + ... where (X_{ref},Y_{ref}) are the object coordinates in the direct image and Y is the center of the trace at the distance $(X-X_{ref})$ along the detector X-axis. The coefficients DYDX_A_n are functions of the position on the detector (see the aXe manual for details).

Figure 2 shows a sum of the direct (F165LP) and prism (PR110L/PR130L) images for PG1322+659. The spectra are found to the left of the direct images, with wavelength increasing from the left to the right. Already in the 2-D images, the Ly α line of the QSO spectrum can be seen slightly to the right of the center of the spectral traces. Unlike the PR200L, the SBC prism spectra show no red “pile-up”, due to the drop in detector sensitivity at wavelengths > 2000Å.

The spectra were traced by measuring the centroid along the image columns as a function of trace distance $(X-X_{ref})$. The observations of the QSO PG1322+659 were used to define the trace descriptions, as these had the best spatial coverage. For PR110L, a linear

fit was found to provide an adequate approximation to the traces, while a quadratic term was included for the PR130L. In both cases, the dispersion direction is aligned with the detector rows to within 1 degree. Some variation across the field was seen. The trace descriptions are summarized in Table 2.

Table 2. Trace descriptions for the SBC prisms. At each position (X_{ref},Y_{ref}), the terms DYDX_A_n are described as DYDX_A_n(X_{ref},Y_{ref}) = a0n + a1n*X_{ref} + a2n*Y_{ref}.

Term	a0n	a1n	a2n
PR110L			
DYDX_A_0	0.99	-1.60E-4	0.002598
DYDX_A_1	-0.0139	1.267E-5	-3.41E-6
PR130L			
DYDX_A_0	4.10	-0.00647	0.003044
DYDX_A_1	-0.0805	-5.27E-5	7.544E-7
DYDX_A_2	-1.99E-4	-1.56E-7	-1.99E-8

The trace descriptions were then inserted into aXe configuration files, input object lists were created for each observation, and the spectra were extracted with aXe. An extraction box width of +/-17 pixels (0.5 arcsec) was used. Since no wavelength calibration had been established at this point, a special aXe calibration file was used for this initial extraction in which the “wavelength” scale was identical to the trace distance.

Wavelength calibration

The QSO spectra were converted from the FITS binary table format output by aXe to IRAF ‘multispec’ format and the centroids of prominent emission lines in the spectra were then measured using the SPLOT task in IRAF. For the lower-redshift QSO (PG1404+226), both Ly α (1335Å) and C IV (1701Å) could be measured, while only the Ly α line (1420Å) could be measured for PG1322+659. Thus, three wavelength sampling points were available to define the dispersion solution. The usual inverse polynomial form (Bohlin et al. 2000) was assumed:

$$\lambda = \mathrm{DLD1P\_A\_1} + \mathrm{DLD1P\_A\_2}/(\Delta X - \mathrm{DLD1P\_A\_0}) + \mathrm{DLD1P\_A\_3}/(\Delta X - \mathrm{DLD1P\_A\_0})^2 + \mathrm{DLD1P\_A\_4}/(\Delta X - \mathrm{DLD1P\_A\_0})^3 + \mathrm{DLD1P\_A\_5}/(\Delta X - \mathrm{DLD1P\_A\_0})^4$$

Here, ΔX is the trace distance and the variation of the coefficients DLD1P_A_0-DLD1P_A_5 across the detector is parameterized in the same way as for the trace descriptions. With only three wavelength sampling points, it was not possible for solve for all the

coefficients and the higher-order terms (DLD1P_A_2 - DLD1P_A_5) were adopted from Bohlin et al. For the DLD1P_A_0 and DLD1P_A_1 terms, we solved directly for the full 2-D solution, rather than fitting each spectrum individually and then fitting the coefficients as a function of (X_{ref},Y_{ref}). In practice this was done by using the AMOEBA routine (Press et al. 1992) to search for values of the coefficients (a00, a10, a20, a01, a11, a21) which minimized the residuals $\Sigma[\lambda_{ref}-\lambda_{obs}(a_{mn}, X_{ref}, Y_{ref}, \Delta X)]^2$ for all observed spectral features at all locations on the detector. With this approach it was straight forward to deal with the different spatial- and wavelength coverage of the two calibrator targets. The resulting best-fit coefficients are listed in Table 3 - note that the higher-order terms are assumed to be constant across the detector area. The fits generally reproduced the reference wavelengths within better than 0.5 pixel, corresponding to a typical accuracy of a few Å. Fitting the DLD1P_A_2 terms yielded values consistent with those in Bohlin et al. (2000), but with large uncertainties.

Figure 3 shows the aXe-extracted spectra of the two QSOs (note that flux calibration has also been applied). For comparison, a redshifted and scaled QSO template spectrum (Zheng et al. 1997) is also shown. The Ly α and C IV emission features are found at the expected locations, and even the weaker Si IV feature at rest wavelength 1400Å is seen (redshifted to 1537Å and 1635Å).

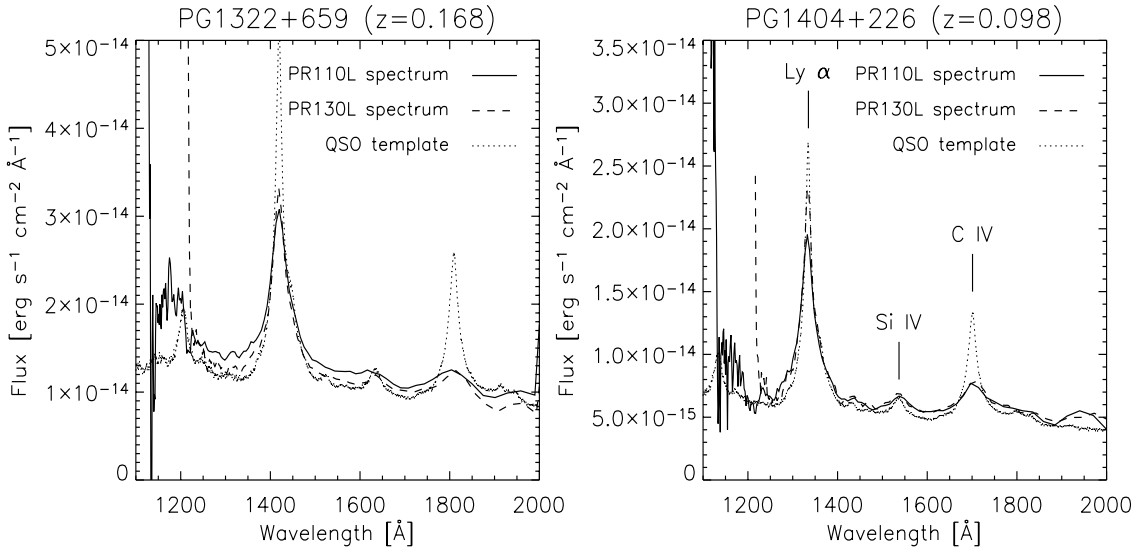

Figure 3: Comparison of aXe-extracted spectra of the two QSOs with a template spectrum (from Zheng et al. 1997) shifted to z=0.098 and z=0.168 and scaled to roughly match the prism spectra.

Table 3. Wavelength solutions for the SBC prisms. The spatial variation of the DLD1P_A_n terms is described by the a0n-a2n terms in a way analogous to that used for the trace description. Note that the DLD1P_A_2-DLD1P_A_5 terms are adopted from Bohlin et al. (2000).

	a0n	**a1n**	**a2n**
PR110L			
DLD1P_A_0	-95.7018	-0.00661906	0.0176038
DLD1P_A_1	1049.39	0.0210533	-0.0186650
DLD1P_A_2	21150.6		
DLD1P_A_3	9.23749e+06		
DLD1P_A_4	4.93403e+08		
DLD1P_A_5	1.24585e+10		
PR130L			
DLD1P_A_0	-80.6079	-0.00711167	0.0154736
DLD1P_A_1	1072.71	0.0124930	-0.0169871
DLD1P_A_2	-14967.6		
DLD1P_A_3	1.94800e+06		
DLD1P_A_4	5.48481e+07		
DLD1P_A_5	1.11636e+09		

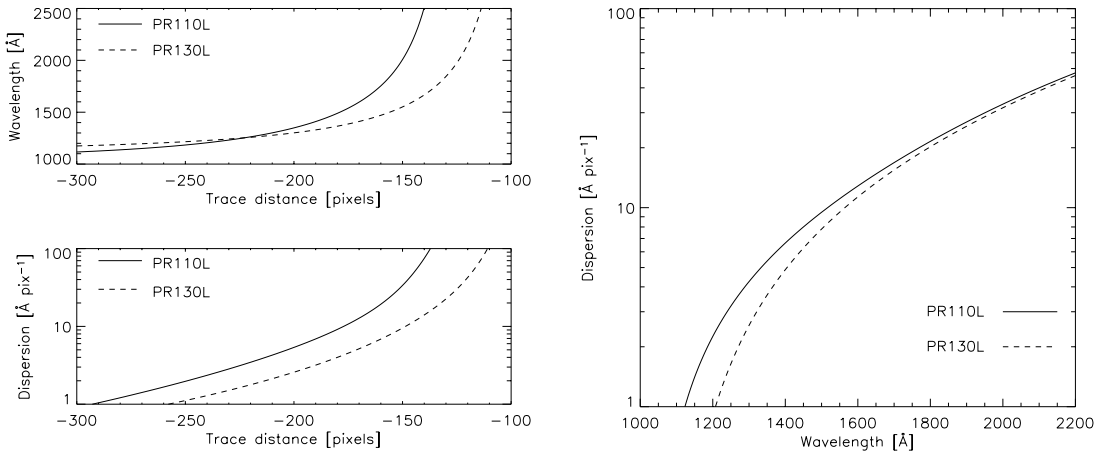

Figure 4: Left: Wavelength and dispersion vs. trace distance. Right: Dispersion vs. Wavelength.

The wavelength scale of the prism spectra is highly non-linear, with spectral resolution decreasing towards longer wavelengths. Figure 4 shows the wavelength and dispersion ($\Delta\lambda/\Delta$pixel) versus trace distance (left) and dispersion versus wavelength (right) for the two prisms. The dispersion varies from about 2Å per pixel at the blue end of the spectra (i.e. a two-pixel resolution element corresponds to $R = \lambda/\Delta\lambda \sim 300$), to ~10Å per pixel at 1600Å (R~80) and is 30Å per pixel at the red end (R~30 at 2000Å).

Flux calibration

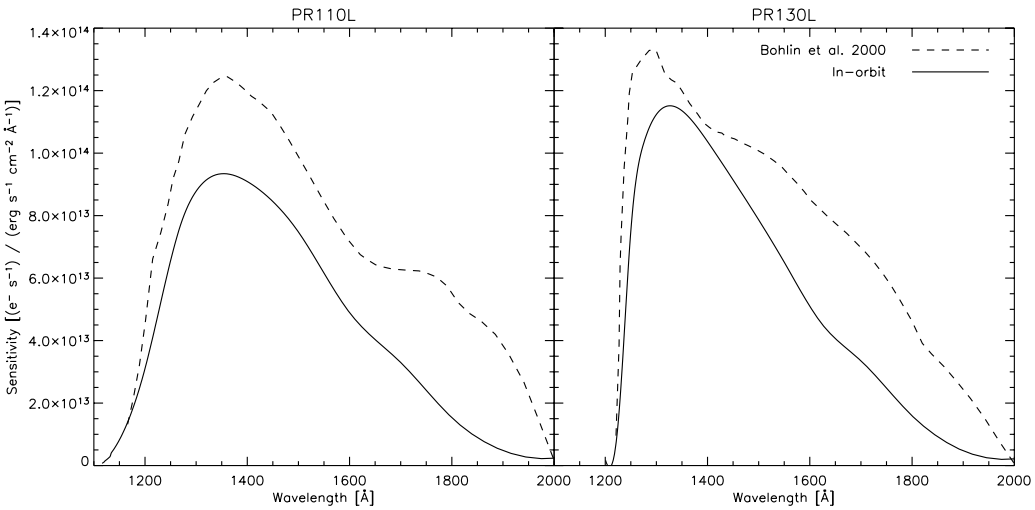

Figure 5: Comparison of sensitivity functions for the SBC prisms derived from the in-orbit calibration (solid curves) and the ground calibration from Bohlin et al. 2000 (dashed curves).

Sensitivity Functions

With the wavelength solution inserted into the aXe configuration files, the spectra of the white dwarf flux standards were extracted using a box of +/-0.5 arcsec and normalized to an exposure time of 1s. For WD1657, a shift was applied to the coordinates measured on the F122M images in order to make them compatible with the trace descriptions, derived with respect to F165LP (see below). The extracted spectra (in units of counts per pixel per sec) were converted to units of counts $Å^{-1}$ s^{-1} and divided by STIS spectra of the standard stars, provided by R. Bohlin. A smooth (spline) function was then fitted to the resulting ratio, and finally all the individual sensitivity curves derived in this way were averaged together to produce the final sensitivity function. At each wavelength bin, the errors on the sensitivity functions were estimated as the mean difference between the averaged sensitivity curves based on each of the two calibrators, or the standard error on the mean of all the individual sensitivity curves, whichever was larger. Figure 5 compares the

sensitivity functions derived here with those shown in Bohlin et al. (2000), derived from the ground calibration data. Generally, the sensitivities derived from the in-orbit calibration are somewhat lower, with the difference being more significant at longer wavelengths and amounting to up to about a factor of 2 at wavelengths longer than 1700Å.

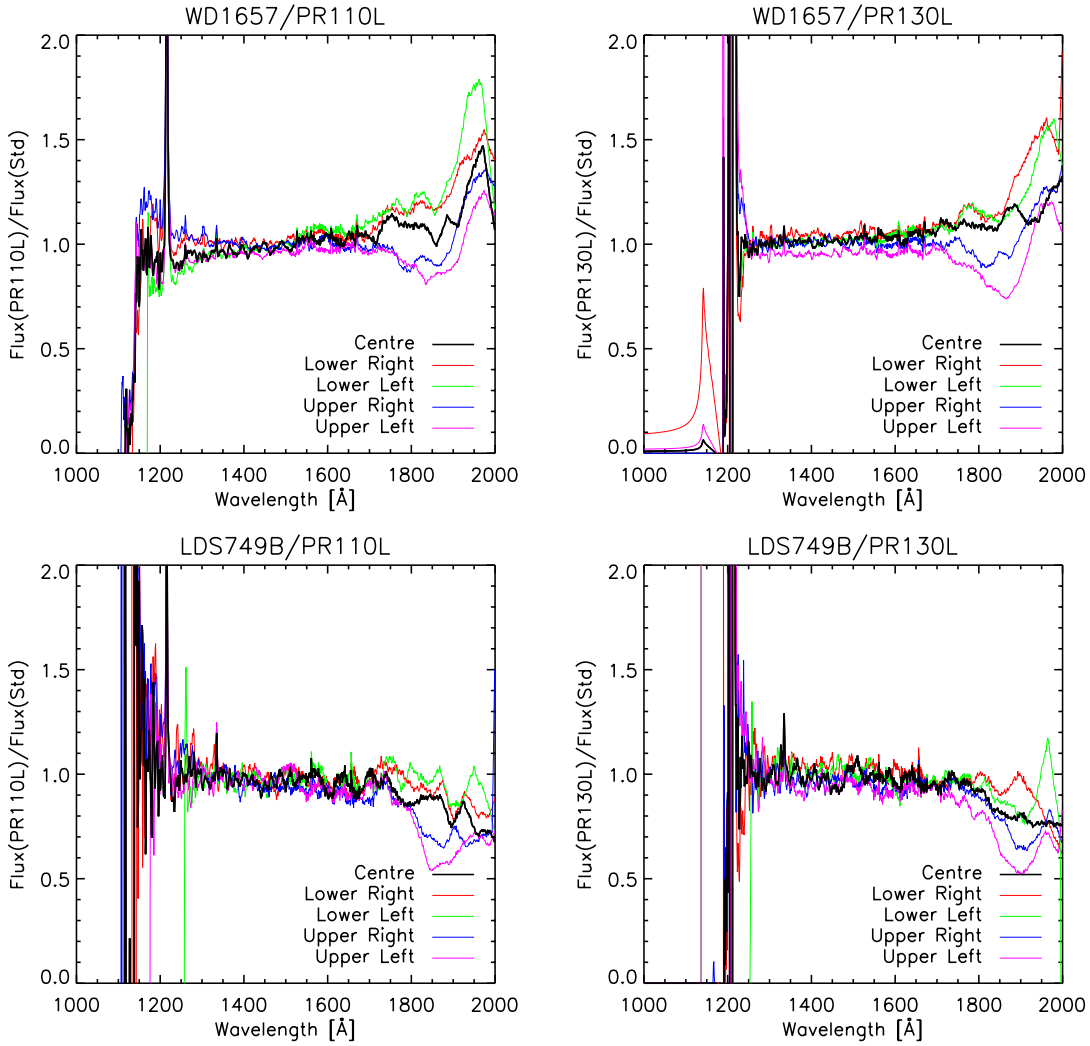

Figure 6: Comparison of the aXe-extracted prism spectra of the two flux standards with the reference spectra. In each panel, the ratio of aXe/standard is shown for 5 different positions on the SBC detector. The spike at the wavelength of Ly α in the PR110L spectra is due to the higher spectral resolution of the reference spectra.

A check of the flux calibration was performed by re-extracting the spectra of the flux standards with aXe and comparing with the STIS standard spectra. This comparison is shown in Figure 6. For wavelengths between 1300Å and 1700Å, the re-extracted spectra agree within about +/-5% with the standard fluxes, while somewhat larger differences are found at the extreme ends of the wavelength range. A spike is seen in the PR110L compar-

ison at the wavelength of Ly α, due to the higher spectral resolution of the standard spectra. Some slight systematic trends are visible, in the sense that the extracted spectra of WD1657 tend to be slightly too red, while the opposite is the case for LDS749B. This may be related to small uncertainties in the wavelength scale, and corresponding conversion from counts per pixel to counts per unit wavelength. This effect is not restricted to the ACS prisms but applies to prism observations in general, due to the non-linear dispersion relations (e.g. Maíz-Apellániz & Bohlin 2005). Note that the biggest differences are seen at long wavelengths where the sensitivity drops rapidly and the dispersion solution becomes strongly non-linear. At 1800Å, an offset of 1 pixel in the wavelength scale corresponds to a change of about 5% in the dispersion, and hence in the counts-per-pixel to counts-per-wavelength conversion. If all objects had intrinsically similar SEDs, these effects would all cancel out, but since the two white dwarfs have rather different SEDs the comparison in Figure 6 provides gives a rough idea about the systematic uncertainties in the flux calibration. However, as seen in Figure 3, the flux calibration appears to work fairly well even for objects with SEDs that are intrinsically quite different from those of the flux standards.

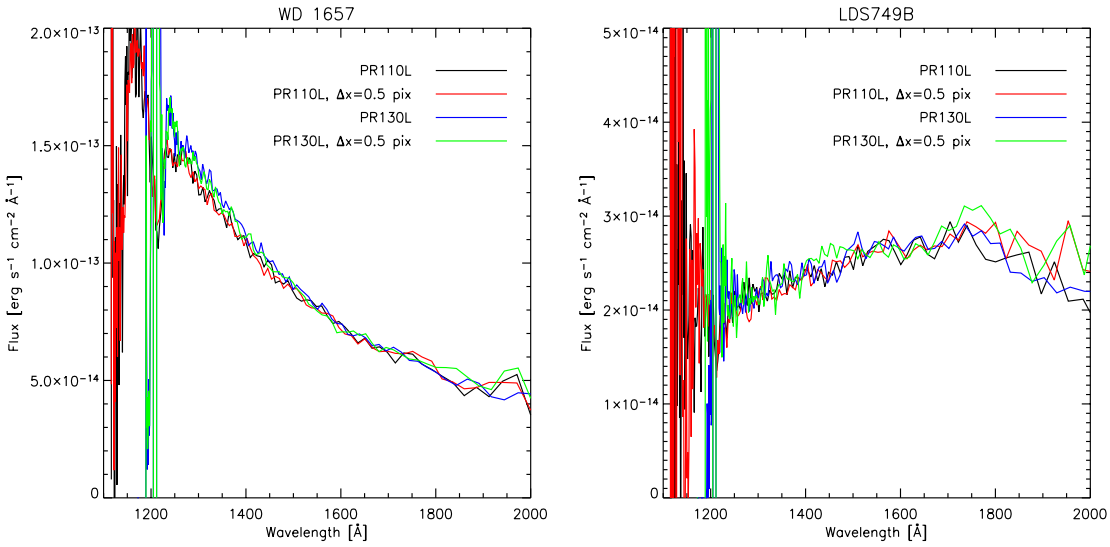

Figure 7: aXe extracted PR110L and PR130L spectra of the two flux standards. For each prism, observations were obtained at two dither positions separated by 0.5 pixels in the x-directions. No systematic difference is apparent between the two dither positions.

In order to quantify the effect of sub-pixel offsets on the flux calibration, exposures were obtained at small (0.5 pixels) dither offsets for the central pointings. Figure 7 compares the PR110L and PR130L spectra (central pointings only) for the two flux standards,

including both the default (POS-TARG = 0) and offset (POS-TARG x = 0.5 pixels) positions. The prism spectra were extracted using the appropriate direct image, i.e. with proper account for the 0.5 pixel offset. As seen from the figure, all four spectra agree within the uncertainties (which can be estimated from the small-scale fluctuations in the flux, since the spectra are intrinsically very smooth) and it thus appears that sub-pixel shifts are not a major source of concern for SBC prism observations.

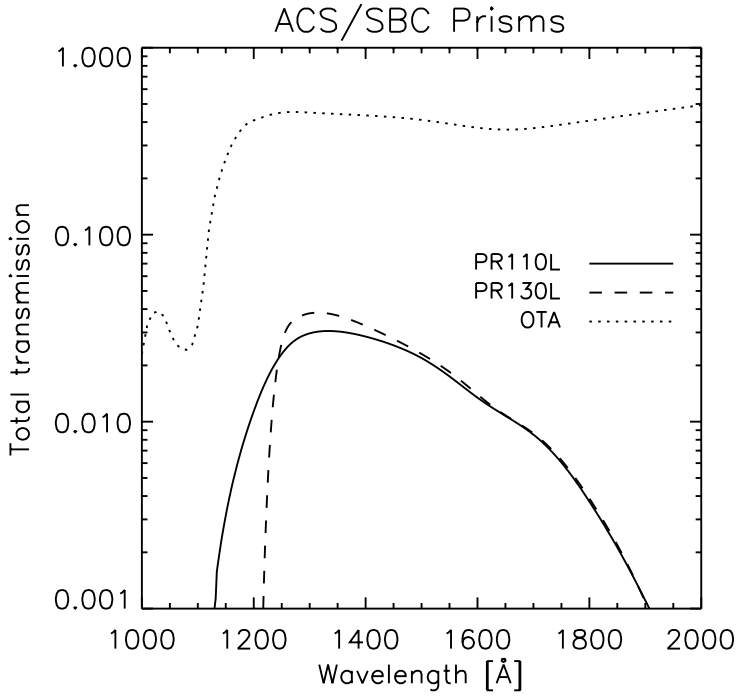

Figure 8: Total throughput of the SBC prisms as derived from the sensitivity curves. For comparison, the throughput of the OTA is also shown.

Finally, from the sensitivity curves it is straight forward to compute the total system throughput for the prism spectroscopy modes, shown in Figure 8. For both PR110L and PR130L this peaks at about 3% at 1300Å, compared to a total OTA (Optical Telescope Assembly) throughput of 45%. Note again that the sensitivity of PR110L extends below 1200Å, while PR130L cuts just redwards of (rest frame) Ly α.

Flat-field cubes

aXe allows for construction of a flat-field cube to correct for sensitivity variations as a function of wavelength as well as spatially. Generally, a flat-field cube uses a polynomial approximation to describe the sensitivity for a given pixel as a function of wavelength, with each layer in the cube having the same dimension as the detector and describing a specific term of the polynomial. The flat-field cube is normally derived from exposures through imaging filters at different wavelengths (Walsh & Pirzkal 2005). As discussed in Mack et al. (2005), pixel-to-pixel sensitivity variations generally show little wavelength dependence for the SBC imaging filters, while some wavelength dependence is seen for the large-scale variations. For prism spectroscopy, the pixel-to-pixel sensitivity variations are corrected by the pipeline. A first-order flat-field cube (i.e. including only the wavelength-independent term) was constructed from the Cycle 13 calibration observations by fitting a two-dimensional second-order polynomial to the total counts in each spectrum as a function of position and then normalizing to a mean of unity. The term “flat-field cube” is used here only to emphasize that the files are designed to be used with aXe - in reality, these are simple 2-D L-flats. Because only the relative fluxes between different pointings were needed, both the white dwarf standards and the QSO spectra could be included. The resulting flats are shown in Figure 9. Both prisms show a similar pattern, with peak-to-peak sensitivity variations of about +/-5% within the useful area of the detector.

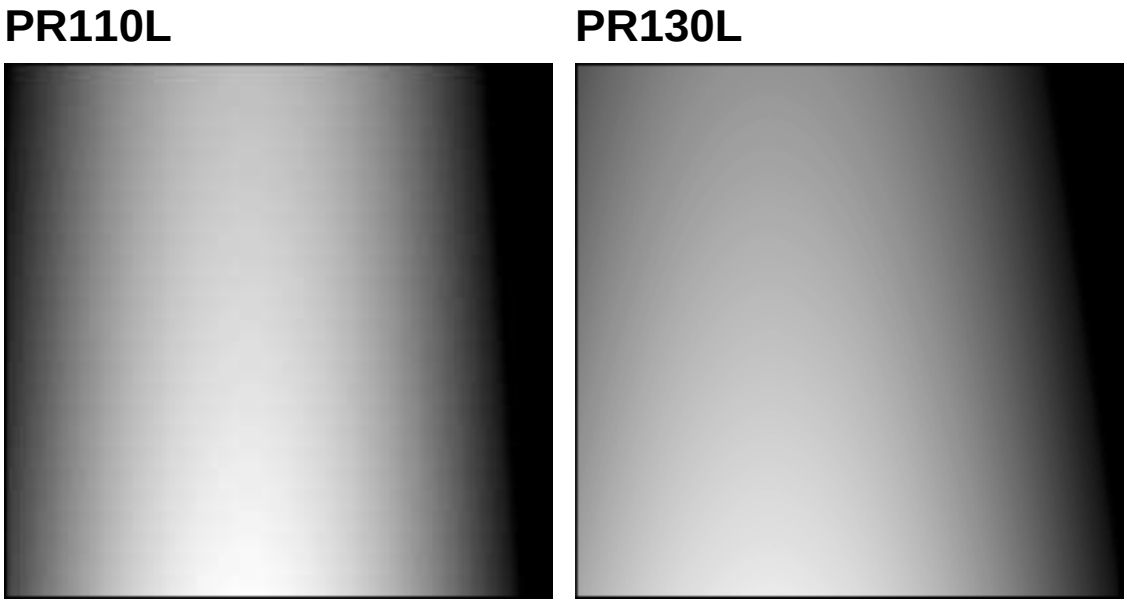

Figure 9: Wavelength-independent flat-fields for the PR110L and PR130L exposures. The lowest and highest intensity levels correspond to factors of 0.90 and 1.05 with respect to the mean sensitivity, respectively. These flat-fields correct for large-scale sensitivity variations across the MAMA detector.

Aperture corrections

Like the ACS (and WFPC2) photometric calibrations, the standard sensitivity files for the SBC prisms refer to an aperture size of +/-0.5 arcsec. However, for some applications it may be desirable to use other aperture sizes. In order to quantify the loss of flux for different aperture sizes, spectra of the flux standards were extracted for a range of aperture sizes and normalized to the fluxes in the default aperture. The normalized flux as a function of aperture size is shown in Figure 10 for three different wavelength ranges (1200Å-1400Å, 1400Å-1600Å, and 1600Å-1800Å). It should be noted that these corrections are only valid for point sources, and will typically be larger for extended objects.

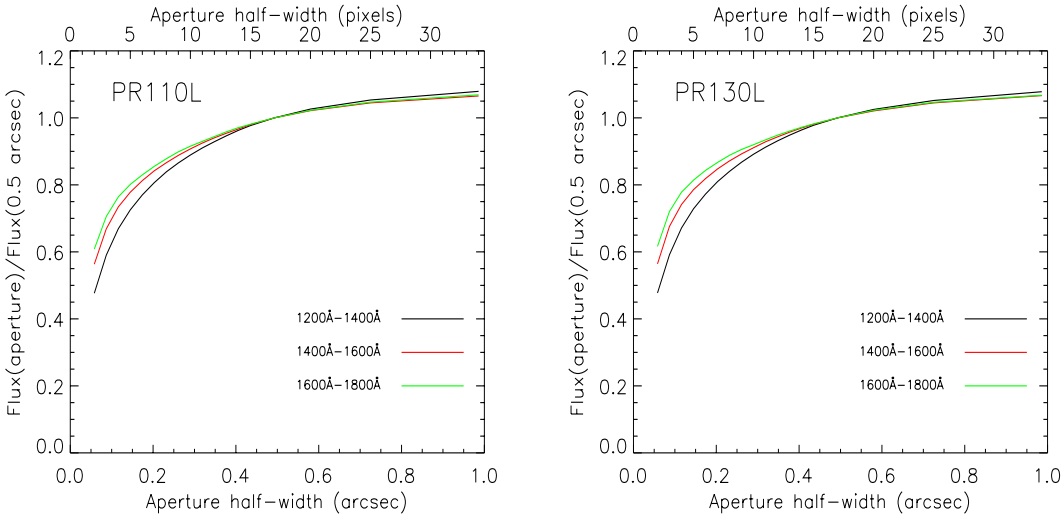

Figure 10: Flux as a function of aperture half-width in pixels and arcsec for a point source. Three different wavelength ranges are shown. The fluxes are normalized to unity for an aperture of +/-0.5 arcsec (+/-17 pixels).

Offsets between direct imaging exposures in different filters

As already noted in previous paragraphs, some offsets were seen between direct imaging exposures obtained in different bands. Comparing the F122M and F165LP exposures of LDS749B, a mean shift of $(\Delta X,\Delta Y) = (X_{F165LP}\text{-}X_{F122M}, Y_{F165LP}\text{-}Y_{F122M}) = (-3.74, 12.07)$ pixels was found, with no indication of a dependence on position on the detector (at the level of 0.1 pixels).

In order to further investigate these offsets, images of NGC 6681 from program 9563 (P.I. de Marchi), taken in the F165LP, F150LP, F140LP, F125LP and F115LP filters were downloaded and analysed. The offsets were determined by comparing the coordinates of several stars in each exposure, measured with the IMEXAMINE task in IRAF. To minimize the risk of pointing errors affecting the measurements, the relative shifts were all measured for exposures obtained within the same orbit. The resulting offsets, relative to

F165LP, are listed in Table 4, and are in the sense that offsets listed in the table should be added to measured coordinates. Offsets amount to up to 12 pixels (0.35 arcsec) in the y-direction and 4 pixels in the x-direction.

Clearly, users observing with the SBC should pay attention to these offsets, which will affect both the centering of the spectral traces within the extraction box (and thus the fluxes) and the wavelength scale. Fortunately, the offsets are easily corrected by simply adding the numbers in Table 4 to any coordinates measured on exposures taken in other filters than F165LP.

Table 4. Offsets between direct imaging exposures in F165LP and other filters.

Filter	X_{F165LP}-X (pixels)	Y_{F165LP}-Y (pixels)
F115LP	-3.74	12.13
F122M	-3.74	12.07
F125LP	0.97	-2.44
F140LP	2.88	-8.48
F150LP	-0.31	1.26
F165LP	0	0

Summary

This ISR has presented in-orbit wavelength and flux calibrations for the SBC PR110L and PR130L prisms.

The wavelength solutions are accurate to a few Å between 1300Å and 1700Å over the SBC field-of-view. While any use of the wavelength solutions beyond this interval formally requires extrapolation of the calibrations derived here, the fits involve only linear terms and it is thus expected that there should be no problems using these solutions over the full wavelength range of the SBC prisms (i.e. ~1200Å - 2000Å). However, observations of two additional QSOs are planned for Cycle 14, which will provide an additional check of the wavelength calibration.

Users should however be aware that the trace- and wavelength solutions derived here are defined with respect to direct images obtained in the F165LP filter. Exposures in other filters show shifts up to 12 pixels in the y-direction and 4 pixels in the x-direction, and object coordinates must be corrected for these shifts before applying the calibrations presented here.

The flux calibrations derived here are expected to be accurate to about 5% over the wavelength range 1300Å-1700Å and across the entire field of view, with slightly larger errors near the extreme ends of the wavelength range (where the sensitivity drops).

The trace, wavelength and flux calibrations presented here are implemented in the standard file formats used by the aXe package, and are available for download via the aXe web page (http://www.stecf.org/software/aXe).

Acknowledgements

I thank H. Kuntschner, M. Kümmel and J. Walsh for many useful discussions throughout this project and R. Bohlin, R. Gilliland, J. Maíz-Apellániz and K. Sembach for helpful comments on the ISR.

References

Bohlin, R. C, Hartig, G., & Boffi, F. R., 2000, *Predicted Sensitivity and Dispersion of the Prisms and Grism*, ISR ACS 2000-001

Kümmel, M., Larsen, S. S., & Walsh, J. R., 2005, *Slitless Spectroscopy with the Advanced Camera for Surveys*, 2005 HST Calibration Workshop, STScI (astro-ph/0512102)

Larsen, S. S., Walsh, J. R., & Kümmel, M., 2006, *Wavelength and Flux calibration of the ACS/HRC PR200L prism*, ISR ACS 2006-XX

Mack, J., Gilliland, R., van der Marel, R., Bohlin, R., 2005, *SBC L-flat Correction and time-dependent Sensitivity*, ISR ACS 2005-13

Maíz-Apellániz, J., & Bohlin, R. C., 2005, *A New Flux Calibration for the STIS Objective Prism*, ISR STIS 2005-01

Pasquali, A., Pirzkal, N., Larsen, S. S., et al., 2006, PASP, in press (astro-ph/0510428)

Press, W. H., Teukolsky, S. A., Vetterling, W. T. & Flannery, B. P., 1992, *Numerical Recipes in Fortran*, Cambridge University Press

Schlegel, D. J., Finkbeiner, D. P., & Davis, M., 1998, ApJ, 500, 525

Veron-Cetty, M. P., & Veron, P., 2003, A&A, 412, 399

Walsh, J. R., & Pirzkal, N., 2005, *Flat-field and Sensitivity Calibration for G800L Slitless Spectroscopy Modes*, ISR ACS 05-02

Zheng, W., Kriss, G. A., Telfer, R. C., et al., 1997, ApJ, 475, 469